Simultaneous analysis of pMHC binding and reactivity unveils virus-specific CD8 T cell immunity to a concise epitope set

Kristensen, Nikolaj Pagh; Dionisio, Edoardo; Bentzen, Amalie Kai; Tamhane, Tripti; Kemming, Janine Sophie; Nos, Grigorii; Voss, Lasse Frank; Hansen, Ulla Kring; Lauer, Georg Michael; Hadrup, Sine Reker

Published in:
Science Advances

Link to article, DOI:
10.1126/sciadv.adm8951

Publication date:
2024

Document Version
Publisher's PDF, also known as Version of record

IMMUNOLOGY

Simultaneous analysis of pMHC binding and reactivity unveils virus-specific CD8 T cell immunity to a concise epitope set

Nikolaj Pagh Kristensen[1], Edoardo Dionisio[1], Amalie Kai Bentzen[1]†, Tripti Tamhane[1], Janine Sophie Kemming[1], Grigorii Nos[1], Lasse Frank Voss[1], Ulla Kring Hansen[1], Georg Michael Lauer[2], Sine Reker Hadrup[1]*

CD8 T cells provide immunity to virus infection through recognition of epitopes presented by peptide major histocompatibility complexes (pMHCs). To establish a concise panel of widely recognized T cell epitopes from common viruses, we combined analysis of TCR down-regulation upon stimulation with epitope-specific enumeration based on barcode-labeled pMHC multimers. We assess CD8 T cell binding and reactivity for 929 previously reported epitopes in the context of 1 of 25 HLA alleles representing 29 viruses. The prevalence and magnitude of CD8 T cell responses were evaluated in 48 donors and reported along with 137 frequently recognized virus epitopes, many of which were underrepresented in the public domain. Eighty-four percent of epitope-specific CD8 T cell populations demonstrated reactivity to peptide stimulation, which was associated with effector and long-term memory phenotypes. Conversely, nonreactive T cell populations were associated primarily with naive phenotypes. Our analysis provides a reference map of epitopes for characterizing CD8 T cell responses toward common human virus infections.

INTRODUCTION

Antigen recognition by CD8 T cells plays a pivotal role in the adaptive immune response to pathogens, autoantigens, and cancer. Characterization and longitudinal monitoring of the antigen-specific immune response, as well as its underlying antigen-receptor repertoire, is therefore an important and necessary endeavor in humans, particularly in light of the protective and therapeutic potential of such immune responses notably in vaccination (*1*–*3*) and cancer immunotherapy (*4*–*8*), respectively.

Exact epitopes of antigen-specific CD8 T cells can be detected either by binding to cognate peptide major histocompatibility complexes (pMHCs) or through a measure of cellular activation in response to antigen stimulation, i.e., "reactivity" (*9*–*14*). However, receptor-ligand binding between a T cell receptor (TCR) and a pMHC complex is not equivalent to T cell reactivity to the given epitope (*15*–*17*). This discrepancy may be attributed to various cell intrinsic and extrinsic factors including co-receptor expression (*18*–*20*), TCR affinity to antigen (*17*, *19*), T cell anergy (*18*, *21*), and chronic antigen stimulation (*22*).

To provide a broad, high-quality map of epitopes recognized in the context of human virus infections, one therefore needs a sensitive yet high-throughput method with integrated information of both pMHC binding and T cell reactivity to peptide. This would allow for simultaneous measurement of cohort-wise prevalence of recognition, magnitude (i.e., cellular frequency), and quality of response (i.e., reactivity) integrated into the same epitope map. Current epitope lists, e.g., Immune Epitope Database (IEDB) (*23*), are based on information from very heterogeneous experimental contexts precluding efficient ranking of epitopes according to observed degree of T cell response prevalence and reactivity.

We therefore integrated the high-throughput assessment of TCR-pMHC binding utilizing DNA barcode-labeled pMHC multimers (*24*) with the determination of T cell reactivity using synthetic peptide pools (*10*, *25*). Here, T cell specificity is assigned based of the barcode-labeled pMHC multimer binding (*24*, *26*, *27*). The total number of TCR-pMHC interactions relevant for a given T cell population can furthermore be assessed through the embedded unique molecular identifiers (UMIs) (*28*). A reduction in TCR surface expression, due to activation-induced down-regulation (*29*–*33*), will therefore lead to a reduced pMHC surface density and hence reduced barcode-associated UMI counts for a given specificity. As such, T cell reactivity, in the form of TCR down-regulation following antigen exposure, can be assigned for each specific T cell population, by measuring the relative loss of signal for a specific barcode associated with its unique pMHC multimer. We then tested epitope binding and reactivity of 10,365 pMHC interactions across 48 donors, allowing us to define 137 high-confidence epitopes across common virus infections along with 2 epitopes from tumor-associated antigens, which form a hierarchy of functional epitope recognition in blood donors and a reference map complete with expected values for prevalence of recognition and reactivity. Moreover, we demonstrate here that nonfunctional T cell characteristics are often linked to T cell phenotypes corresponding to either lack of antigen exposure (i.e., naïve T cells) or immunosenescence ($CD57^{hi}$ Temra cells) and that certain epitopes frequently drive such nonfunctional T cell responses.

RESULTS

Diminished pMHC-multimer binding is an early and sensitive marker of T cell reactivity

TCR down-regulation and the associated decreased pMHC multimer staining of recently activated antigen-specific CD8 T cells have been

[1]Section for Experimental and Translational Immunology, Department of Health Technology, Technical University of Denmark (DTU), Kongens Lyngby, Denmark. [2]Liver Center and Gastrointestinal Division, Department of Medicine, Massachusetts General Hospital and Harvard Medical School, Boston, MA 02114, USA.
*Corresponding author. Email: sirha@dtu.dk
†Present address: University College London, Cancer Institute, London, UK.

documented for both high- and low-avidity ligands in the OT-I and 2C TCR transgenic systems (*32*). Similar observations have been made ex vivo in a human setting using selected epitopes derived from human cytomegalovirus (CMV) and influenza virus (FLU) antigens (*33*). We explored this phenomenon in detail for a variety of well-described viral epitopes using human PBMCs. We observed strongly decreased median fluorescent intensities (MFIs) and decreased frequencies of pMHC multimer positive T cell populations following 24-hour peptide stimulation across all virus-derived epitopes tested (Fig. 1, A to C, and fig. S1A). This coincided with the up-regulation of canonical activation markers $CD69^+$ and $CD137^+$ [activation-induced markers (AIMs)] (*10*, *12*) (Fig. 1, A and D). Furthermore, dilution of the stimulating peptide showed a clear dose dependency (Fig. 1E and fig. S1, B and C). Finally, we performed a time series to map the temporal kinetics of the effects of peptide stimulation in the context of different antigen-specific populations from the same donor. We observed a decrease in pMHC multimer binding specific to the targeted CD8 T cell response as early as 3 hours after stimulation, with the strongest effect at 24 to 48 hours. We moreover found no evidence of renewed capacity to bind pMHC multimers at 48 hours after stimulation (Fig. 1F and fig. S1, D to G). $CD137^+$ kinetics were largely similar to previously published reports (fig. S1H) (*12*), although we observed a tendency for marked background staining of anti-CD137 particularly at early time points (fig. S1I). In summary, we confirm reduction in pMHC multimer binding to T cells as a specific and sensitive readout for productive TCR engagement in vitro.

Peptide stimulation correlates with loss of pMHC multimer binding measured by DNA barcode counts in antigen-specific CD8 T cell populations with negligible bystander effects

To scale our experimental workflow of assessing both T cell epitope binding and reactivity simultaneously (Fig. 2A) to hundreds of epitopes using DNA barcode-labeled multimers, we selected 945 epitopes from 29 different common viruses (table S1) restricted to 25 human leukocyte antigen (HLA) alleles from IEDB (selection details in Materials and Methods). Epitopes were selected to represent viruses with frequent exposure in healthy populations. The epitope library was characterized by a predominance of herpesvirus epitopes as well as HLA-A*02:01 restricted peptides (Fig. 2B and fig. S2A). As a reference, the library also included two epitopes derived from well-known tumor-associated self-antigens, $MART1_{26–35(Leu27)}$ ELAGIGILTV and $NY\text{-}ESO_{157–165}$ SLLMWITQV restricted to HLA-A*02:01 (*34*, *35*).

We verified that activation-induced TCR down-regulation and reduction in pMHC multimer staining intensity was (i) measurable by DNA barcodes used to tag individual pMHC multimers and (ii) unaffected by activation of other antigen-reactive CD8 T cells (i.e., bystander activation). To do this, we included a wide panel of DNA barcode-labeled pMHC multimers encompassing 36, 96, and 59 virus epitopes restricted to HLA-A*01:01, A*02:01, and B*08:01, respectively. We split PBMCs from three healthy donors into unstimulated, partially stimulated, and fully stimulated short-term cultures, and stained each culture in triplicates with donor-specific, HLA-matching pools of barcoded multimers. Amplicon sequencing of the pMHC multimer-associated barcodes was subsequently performed on $multimer^+$ CD8 T cells, and individual enrichment scores for TCR:pMHC binding were calculated based on such barcodes. As expected, we observed loss of fluorescent pMHC multimer binding when using HLA-A*01:01-, A*02:01-, or B*08:01-restricted peptide pools (Fig. 2C and fig. S2B) and a corresponding increase of CD137 expression (fig. S2C). Furthermore, we observed that cognate peptide stimulation resulted in decreased enrichment scores (masked log2FC) for specific pMHC multimer binding, while T cell populations specific for other epitopes in the same sample were unaffected by such stimuli (Fig. 2, D and E). In total, 70 epitope specificities were assessed from three donors, and the majority of epitopes (54 of 70) were significantly affected by peptide stimulation (Fig. 2D and fig. S2, D and E). Next, we scaled our methodology to the final panel of 929 epitopes (see Materials and Methods for excluded epitopes) and evaluated T cell responses in 48 donors (27 healthy blood donors and 21 donors recently or chronically infected with hepatitis virus). Peptides were grouped and pooled according to HLA restrictions as reported in IEDB and recombined on the day of stimulation into donor-specific peptide pools covering up to six HLA class I alleles for any given donor. DNA barcode-labeled MHC multimers were also grouped according to HLA and combined into donor-specific multimer pools. All multimer-binding T cells were then sorted to determine donor-specific T cell responses (Fig. 2F and fig. S2F). While donor-to-donor variations were observed, the increase of AIM^+ CD8 T cells in stimulated samples corresponded to the observed decrease of multimer-specific CD8 T cells ($R = 0.8$, $P < 2.2 \times 10^{-16}$) (Fig. 2G). Furthermore, the general increase in CD137 MFI values also corresponded to decreased multimer fluorescent intensities ($R = 0.6$, $P = 5.7 \times 10^{-4}$) (fig. S2G).

Overall, these data establish that an assay combining pMHC multimer staining with peptide stimulation can be used to simultaneously test hundreds of distinct T cell specificities with DNA-barcoded pMHC multimer libraries and determine T cell antigen reactivity with negligible bystander effects.

Evaluation of pMHC binding and antigen reactivity for large epitope libraries identifies a hierarchy of antigen-specific CD8 T cells with different reactivity levels

Next, we assessed TCR down-regulation for individual antigen-specific CD8 T cell responses across our cohort, by accounting for decreased UMI counts for a given pMHC-associated barcode. We studied a total of 10,365 pMHC interactions and identified 647 epitope-specific CD8 T cell populations in unstimulated samples. We estimated the underlying frequency of epitope-specific CD8 T cells by weighting the total $multimer^+$ population of CD8 T cells observed by flow cytometry according to the fraction of mapped UMIs pertaining to the given epitope (*4*, *24*), which resulted in an estimated frequency range of 0.0005% to 18.7% of total CD8 T cells in unstimulated samples. All identified responses across the total cohort are depicted in Fig. 3A (upper panel, unstimulated sample), each dot representing one multimer-specific population in a given donor based on significantly enriched pMHC barcodes. Parallel assays after epitope peptide pool stimulations (Fig. 3A, lower panel) revealed a concomitant partial binding loss across a wide range of T cell specificities targeting different epitopes and viruses. Delta log 2 fold change values (Δlog2FC) were subsequently calculated comparing paired multimer data from unstimulated and stimulated samples, where negative Δlog2FC generally represents decreased barcode enrichment and multimer binding (i.e., reactivity) and positive values indicate unchanged binding. T cell populations assigned with antigen reactivity ($\Delta log2FC < 0$) are shown as circles, while nonreactive populations ($\Delta log2FC > 0$) are shown as triangles (Fig. 3A). In total, 564 of the 647 identified epitope-specific populations were assigned with a net negative Δlog2FC after stimulation,

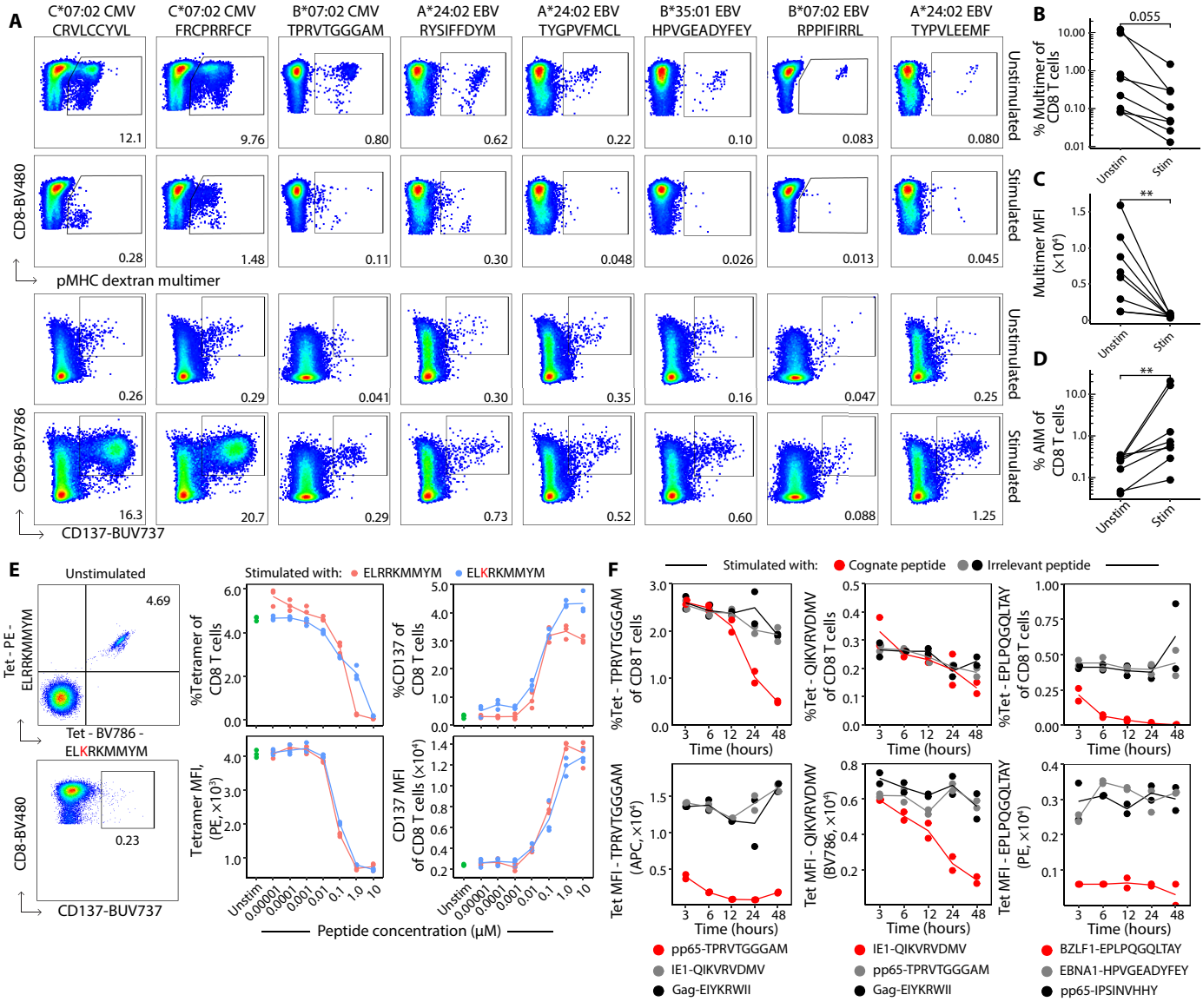

Fig. 1. Diminished intensity of pMHC multimers is an early and sensitive marker of T cell activation. (**A**) Loss of dextran pMHC multimer-staining following peptide-based stimulation of antigen-specific CD8 T cells and concomitant increase in frequency of $CD69^{+}CD137^{+}$ CD8 T cells. PBMCs were stimulated with 1 μM peptide for 24 hours. Unstimulated controls were treated with equimolar DMSO. Samples were pregated for live $CD14^{-}CD19^{-}CD3^{+}CD4^{-}CD8^{+}$ lymphocytes. Responses from three different donors were investigated. Each response was investigated once. (**B** to **D**) Statistics pertaining to (A). (B) Multimer frequency of CD8 T cells, (C) multimer MFI, and (D) AIM frequency, i.e., frequency of $CD69^{+}CD137^{+}$ of CD8 T cells. (**E**) Limiting dilution of two 24-hour stimulation series in triplicates. Unstimulated controls were treated with 10 μM DMSO. $Tetramer^{+}$ cells were pregated on live $CD3^{+}CD4^{-}CD8^{+}$ lymphocytes. Tetramer MFI and frequency were measured. Tetramer MFI for ELKRKMMYM-BV786 is shown in fig. S1C. (**F**) Time series spanning 3 to 48 hours of stimulation with 1 μM peptide in duplicates. Each time series was stimulated with one cognate peptide (red) and subsequently stained with three tetramers including two irrelevant peptides (gray and black) in addition to the cognate peptide. $Tetramer^{+}$ cells were pregated on live $CD3^{+}CD4^{-}CD8^{+}$ lymphocytes. Tetramer-null controls were used as gating controls (see fig. S1D). Representative flow plots are shown in fig. S1 (E and F). Two additional positive peptides are presented in fig. S1G. *P* values were calculated using a paired Wilcoxon test. $^{**}P < 0.01$. MFI, median fluorescent intensity. AIM, activation-induced marker. Experiments were performed once.

whereas 83 responses were assigned with positive or unchanged Δlog2FC values (Fig. 3B).

To generate discrete categories of TCR reactivity that take into account areas of technical uncertainty, we regarded $-\Delta\log2FC > 0.75$ as "reactive" epitope recognition, $-0.75 < -\Delta\log2FC < 0.75$ as a "mixed" population of reactive and nonreactive epitope recognition, and $-\Delta\log2FC < -0.75$ as "nonreactive" epitope recognition. This allowed us to visualize and rank epitope-specific recognition according to measured TCR down-regulation and loss of pMHC multimer binding across multiple independent donors (Fig. 3C). Examples of highly reactive populations (indicated by numbers on Fig. 3C) included B*35:01-restricted BZLF1-EPLPQGQLTAY from Epstein-Barr virus (EBV, mean estimated frequency: 0.26%), A*02:01-restricted E1A-LLDQLIEEV from human adenovirus C (HAdV-C, mean estimated

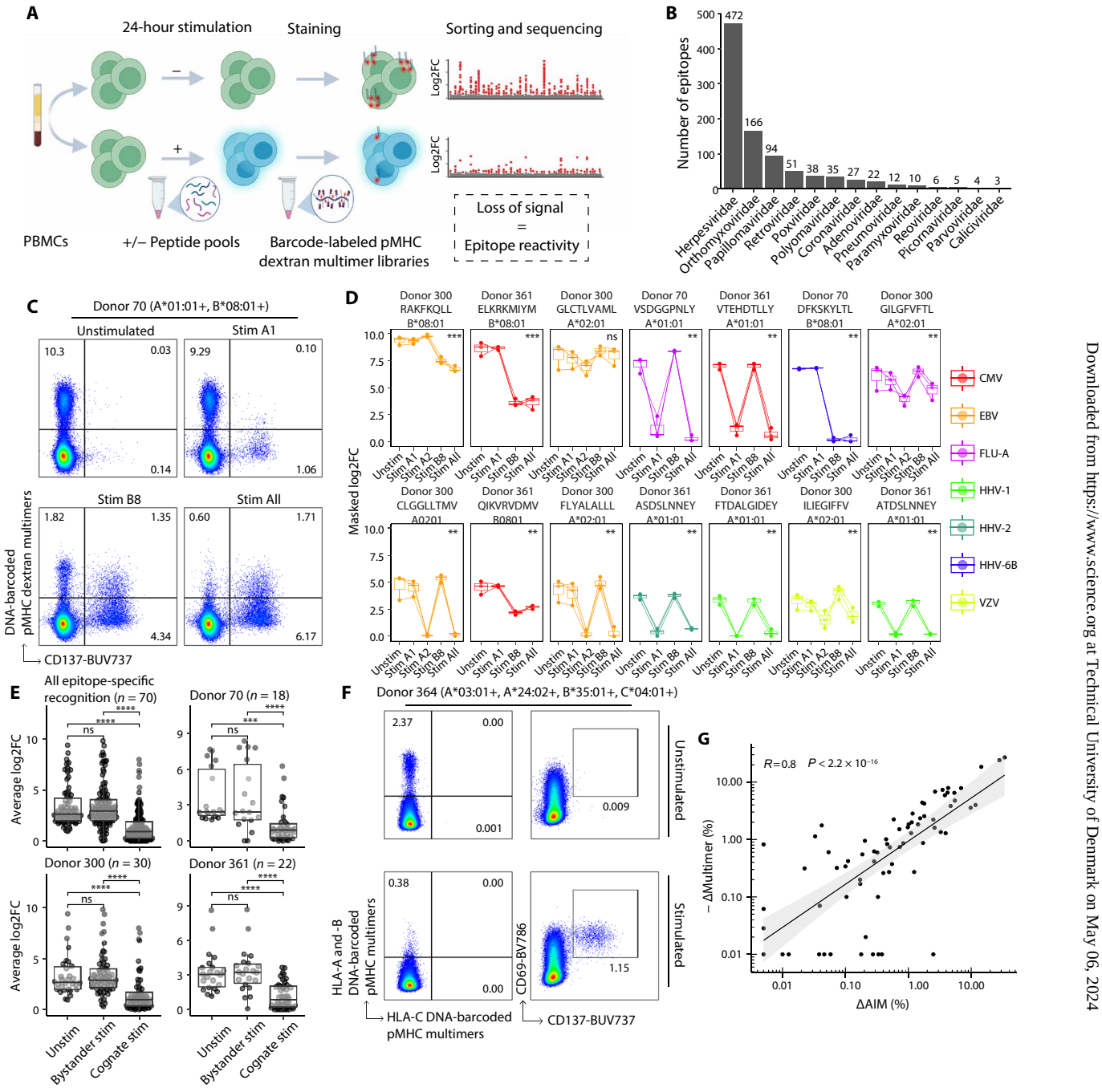

Fig. 2. Multiplexing pMHC multimers using DNA barcodes allow monitoring of specific activation following peptide pool-based stimulation. (**A**) Biorender experimental flow chart. (**B**) Multimer-library size per virus families selected from IEDB (*23*). (**C** and **D**) Multimer-binding following 24-hour stimulation in three donors. (C) Representative cell sorts of antigen-specific CD8 T cells using barcode-labeled pMHC multimers. Cells were sorted from upper quadrant gates. Stim A1, Stim B8, and Stim All refer to pool-based stimulations with 36 A*01:01-restricted peptides, 50 B*08:01-restricted peptides, and the collective pool of 86 peptides, respectively. All conditions were recorded in technical triplicates. (D) Enrichment scores for select multimer-specific CD8 T cells across three donors and three to four stimulatory settings. Stim A2 refers to the pool-based stimulations with 96 A*02:01-restricted peptides. Samples were pregated for live $CD14^-CD19^-CD3^+CD4^-CD8^+$ lymphocytes. See all remaining populations in fig. S2 (F and G). (**E**) Seventy virus-specific populations were grouped according to whether the respective stimulatory setting included the peptide used for multimer-generation (cognate stim) or not (bystander stim). (**F**) PBMCs from 48 donors were individually stimulated with pools restricted to one to six donor-derived HLA alleles. $Multimer^+$ CD8 T cells were sorted and barcodes sequenced (Fig. 3). Samples were pregated on live $CD14^-CD19^-CD3^+CD4^-CD8^+$ lymphocytes. Additional flow cytometry is available in fig. S2H. (**G**) Correlation between observed change in multimer frequency [Δmultimer (%)] and change in $CD69^+CD137^+$ frequency [ΔAIM (%)] upon stimulation. The shaded area is the 95% confidence interval. Spearman correlation was used. Unpaired Wilcoxon test between grouped unstimulated/bystander and cognate stimulated samples was performed in (D). *P* values were calculated using Dunn's test in (E) and adjusted using Benjamini-Hochberg. Boxplot bounds are 25th and 75th percentiles along with the median. Upper and lower whiskers span the range of data up to 1.5× of the IQR. $^{**}P < 0.01$, $^{***}P < 0.001$, $^{****}P < 0.0001$; ns, not significant. All experiments were performed once.

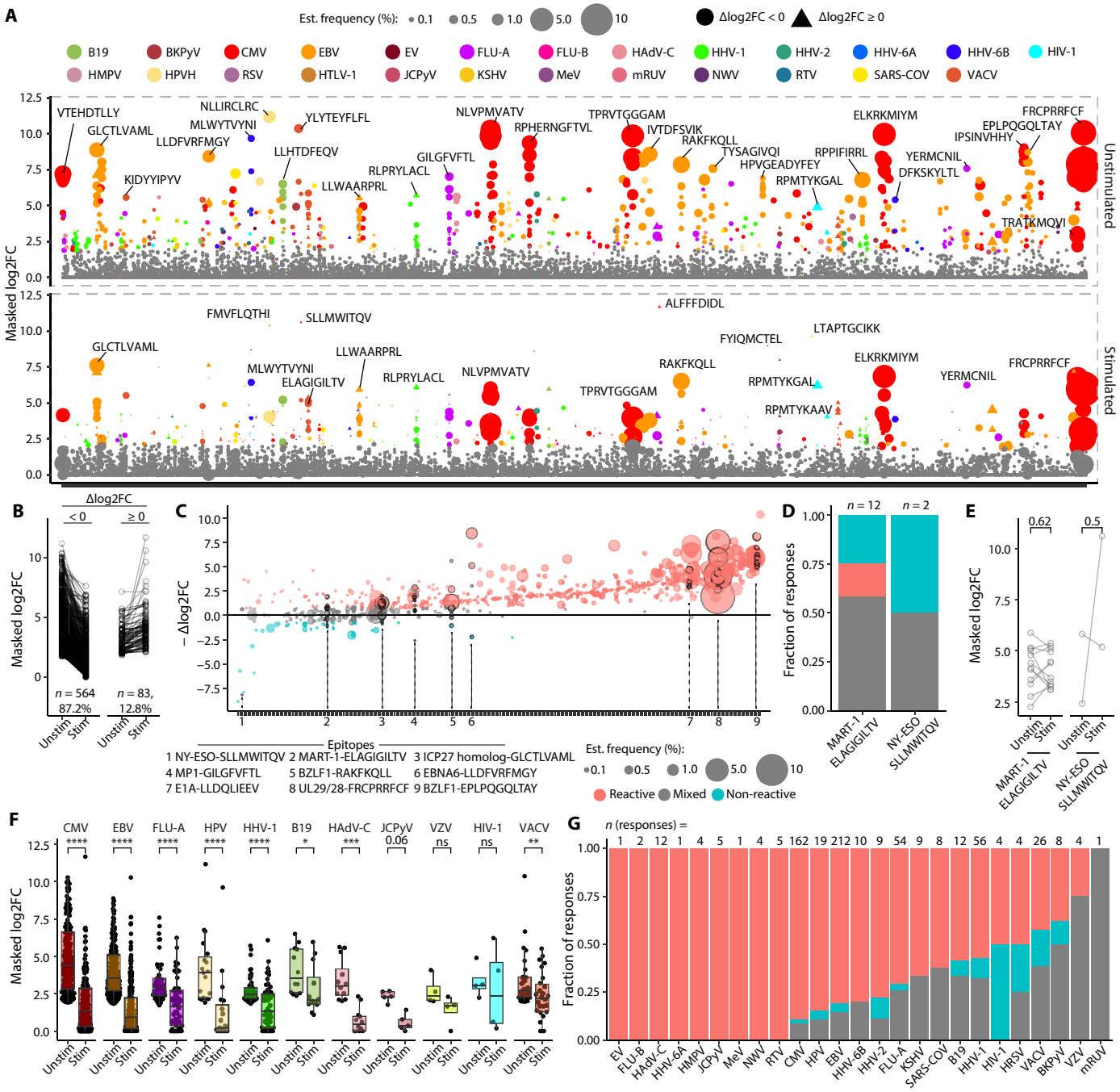

Fig. 3. Simultaneous evaluation of epitope binding and reactivity for large epitope libraries captures a hierarchy of antigen-specific CD8 T cells with heterogeneous antigen reactivity. (**A**) Compiled epitope recognition for 48 donors. Detectable T cell populations are colored corresponding to their virus of origin. The size of the dots denotes the estimated frequency of the underlying epitope-specific CD8 T cells. (**B**) Barcode enrichment scores comparing unstimulated samples to stimulation samples. (**C**) Epitope recognition including underlying estimated frequency (dot size) depicted according to the observed reactivity score (−Δlog2FC). Each epitope and corresponding epitope-specific populations are ranked on the horizontal axis according to average Δlog2FC and grouped in three bins: −Δlog2FC > 0.75 ("Reactive"), −0.75 < −Δlog2FC < 0.75 ("Mixed"), and −Δlog2FC < −0.75 ("Nonreactive"). Notable responses are highlighted with black borders and their identities were specified on the bottom axis. (**D**) Proportion of reactive, mixed, and nonreactive CD8 T cell recognition toward tumor-associated epitopes restricted to HLA-A*02:01. Numbers above each column denote the total number of independent responses discovered for each epitope specificity. (**E**) Barcode enrichment scores for each of the CD8 T cell populations recognizing tumor-associated epitopes, in the unstimulated versus stimulated condition. (**F**) Pairwise comparison of barcode enrichment scores following stimulation for representative virus origins (see fig. S3D for all virus groups). (**G**) Proportion of reactive, mixed, and nonreactive epitope recognition among virus-specific CD8 T cells across all donors. Numbers above each column denote the total number of independent responses discovered for each virus origin. *P* values in (E) and (F) were calculated using paired Wilcoxon test. Boxplot bounds show the 25th and 75th percentiles along with the median. Upper and lower whiskers span the range of data up to 1.5× of the IQR. *$P < 0.05$, **$P < 0.01$, ***$P < 0.001$, ****$P < 0.0001$. Experiments were performed once.

frequency: 0.23%), and C*07:02-restricted UL29/28-FRCPRRFCF from CMV (mean estimated frequency: 7.16%). Examples of nonreactive populations featured recognition of A*02:01-restricted NY-ESO-SLLMWITQV (mean estimated frequency: 0.02%) and to some extent MART1-ELAGIGILTV (mean estimated frequency: 0.11%), which were detected in 2 and 12 independent donors, respectively (Fig. 3, D and E).

To explore reactivity hierarchies between T cell responses targeting different viruses, we grouped T cell recognition of epitopes derived from the same virus together and compared their overall enrichment scores as well as their frequency of reactive, mixed, and nonreactive response patterns (Fig. 3, F and G, and fig. S3A). A significant reduction in barcode enrichment scores were found for a range of viruses including EBV, CMV, FLU-A, human papillomavirus (HPV), herpes simplex virus 1 (HHV-1), B19 parvovirus (B19), HAdV-C, JC polyomavirus (JCPyV, $p = 0.06$), vaccinia virus (VACV), Kaposi's sarcoma-associated herpesvirus (KSHV), human metapneumovirus (HMPV), human herpesvirus 6B (HHV-6B), severe acute respiratory syndrome coronavirus (SARS-COV), and rotavirus A (RTV, $p = 0.06$) (fig. S3A). However, when taking into account donor-specific heterogeneity, we found that VACV, HHV-1, BK Polyomavirus, and HIV-1 in particular showed a bimodal distribution, with reactivity assigned only in approximately half of the donors (Fig. 3G).

In summary, our methodology enabled large-scale discovery of virus-specific CD8 T cells across a cohort of PBMC donors, revealing a reactivity hierarchy between virus infections.

A reference map of high-confidence virus-derived CD8 T cell epitopes and their associated antigen reactivity

Ranking epitope recognition by measured antigen reactivity adds important additional information when generating reference maps of epitopes recognized in cohorts of interest. To derive a reference map of high-confidence CD8 T cell virus epitopes from common virus infections in our donors, we selected all epitopes recognized in at least two independent donors and ranked them according to the proportion of reactive, mixed, and nonreactive epitope-specific CD8 T cell populations among the detected responses (Fig. 4 and tables S2 and S3). In total, we report 137 virus epitopes, out of which 84% (115 epitopes) featured reactivity to peptide stimulation in ≥50% of cases. Sixteen epitopes were dominated by T cell responses with mixed reactivity. Finally, we observed that EBNA4-RAKFKQLL, LMP2-RRRWRRLTV, EBNA-1-FVYGGSKTSL, ICP22-APRIGGRRA, LMP2-PYLFWLAAI, and D1-RPSTRNFFEL were more heterogeneous, with no single of the three categories exceeding 50%. We present data on cohort-wide antigen reactivity in Fig. 4 as a heatmap and in a tabular format in tables S2 and S3 along with the prevalence of CD8 T cell recognition across our cohort, the average population frequency observed in peripheral blood, the number of IEDB reports associated to a given epitope, the average "reactivity score" Δlog2FC, and the predicted MHC binding affinity for each epitope (netMHCpan v. 4.1) (*36*).

Consistent with previous reports on impaired priming (*37*), maintenance (*38*, *39*), and memory formation (*40*) for bystander virus-specific CD8 T cells during chronic virus infection, we observed that donors recently or chronically infected with hepatitis virus exhibited reduced frequency of bystander virus-specific CD8 T cells compared to healthy donors. This effect was observed in an HLA-diverse setting (fig. S3, B and C), but was particularly pronounced for EBV, FLU-A, and HHV-1 infection in an HLA-A*02:01-controlled setting where CMV-specific CD8 T cells also exhibited a tendency for reduced

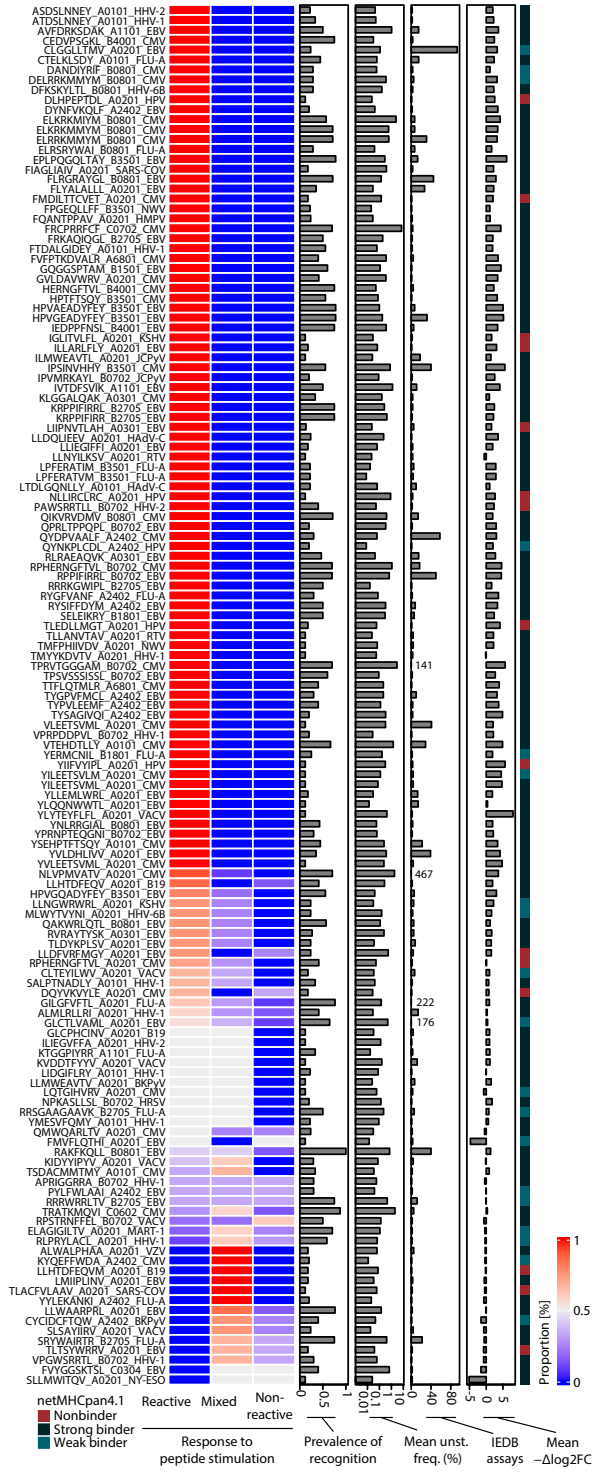

Fig. 4. Common virus epitopes associated with reactivity and nonreactivity. Heatmap denoting proportion of reactive, mixed, or nonreactive epitope-specific CD8 T cell populations for each specificity. Only T cell epitopes recognized by at least two independent donors are depicted. Additional panels denote prevalence of detection in our cohort, the average response frequency observed in unstimulated control samples, the number of previous positive IEDB assay reports associated with epitope recognition, and the mean reactivity score (−Δlog2FC), respectively. The rightmost colored boxes denote predicted pMHC-binding calculated by netMHCpan4.1 (*36*) for each epitope.

peripheral frequency (fig. S3D). Age defined as two age groups, young adult (age ≤ 30 years) versus old adult (age ≥ 60 years), did not generally affect the median observed frequency of virus-specific CD8 T cells within hepatitis virus-infected donors (fig. S3, E and F). Age and sex were not accessible for anonymous healthy blood donors. In summary, we find that bystander CD8 T cells exhibit reduced frequency during hepatitis virus infection.

CMV- and EBV-specific CD8 T cell populations were overall larger as indicated by median frequencies of 0.14% and 0.09%, respectively, compared to FLU-A–, HHV-1–, and KSHV-specific CD8 T cell populations with median frequencies at 0.03%, 0.04%, and 0.03% (Fig. 5A), respectively, supporting previous findings (*41*). CMV-specific CD8 T cells were also detected at a statistically higher frequencies than HPV and polyoma-specific CD8 T cells, although the latter entailed too few observations to adequately estimate the *P* value. Epitope-specific CD8 T cells targeting VACV, B19, HadV-C, and HHV-6B were present at similar median frequencies as CMV and EBV at 0.07%, 0.09%, 0.1%, and 0.13%, respectively (Fig. 5A). We also summarized the number of high-confidence epitopes found for each HLA allele. As expected, because of the large number of IEDB-derived candidate epitopes restricted by HLA A*02:01, most of the identified 137 virus epitopes in our screening were restricted by this allele (Fig. 5B and fig. S2A). These data establish a reference map of virus-specific CD8 T cells based on a large library of viral antigens across multiple viruses and HLA alleles.

Among the 137 high-confidence epitopes, for which T cell recognition was detected, several were minimally described in IEDB (Fig. 5, C and D). This was furthermore visible from the numerically significant yet weak correlation between IEDB assay reports and observed prevalence of reactivity ($R = 0.26$ to 0.30, Fig. 5E).

Together, we report recognition of 137 common virus epitopes along with corresponding antigen reactivity, prevalence, and mean frequency of T cell recognition, by comparing all epitopes in a single experimental framework.

Differences in antigen reactivity reflect co-receptor expression and effector differentiation

To investigate phenotypic characteristics of reactive and nonreactive responses, we selected 12 donors for verification using conventional pMHC tetramers and immunophenotyping including specificities from CMV, EBV, FLU-A, B19, varizella-zoster-virus (VZV), HAdV-C, HHV-1, HHV-6B, and MART-1. We ranked each donor-derived T cell response according to reactive, mixed, and nonreactive categories introduced in Fig. 3. Up to six specificities were encoded per staining reaction using up to two fluorescent tetramers (Fig. 6A). We found that virus-specific CD8 T cell frequencies assessed using conventional tetramers closely matched with the estimated frequencies acquired from the initial barcoded pMHC multimer screens ($R = 0.7$, $P = 3.5 \times 10^{-10}$) (Fig. 6B). Interestingly, we observed pronounced phenotypic heterogeneity between epitope-specific T cells recognizing different virus antigens of interest (Fig. 6, C and D, and fig. S4, A and B). Epitope-specific CD8 T cells recognizing CMV and B19 infections were, for example, dominated by effector memory T cells (Tem, $CCR7^{-}CD45RA^{-}$), whereas epitope-specific CD8 T cells recognizing FLU-A, HAdV-C, and HHV-1 exhibited central memory (Tcm, $CCR7^{+}CD45RA^{-}$)

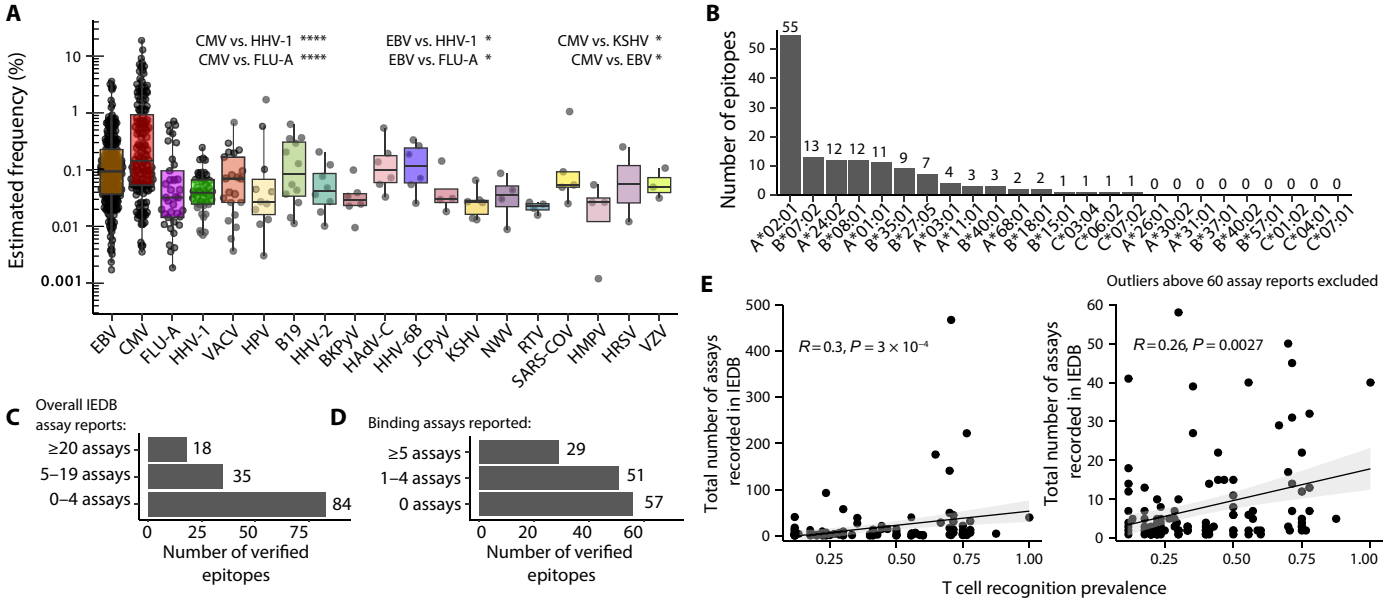

Fig. 5. Common virus epitopes associated with reactivity and nonreactivity. (**A**) Estimated frequency in unstimulated samples for all responses detected across 48 donors grouped by virus origin. (**B**) Number of commonly recognized epitopes per HLA. (**C**) Number of commonly recognized epitopes grouped in three bins according to number of reported assays in IEDB at the time of epitope selection. Structural assays such as x-ray crystallography were excluded from this count (see Materials and Methods). (**D**) Number of epitopes associated with minimal reactivity grouped in three bins according to number of reported qualitative binding assays in IEDB including pMHC multimers. (**E**) Correlation between observed prevalence and IEDB assay reports for all 109 epitopes associated with common reactivity. The shaded area represents the 95% confidence interval. Left: All data. Right: Outliers with extreme number of reports were exclude (above 65 assays). All metrics from IEDB stem from the original database search in October 2020. Correlations and associated *P* values were calculated using Spearman correlation. *P* values were calculated in (A) using Dunn's test and adjusted using the Benjamini-Hochberg method. Boxplot bounds show the 25th and 75th percentiles along with the median. Upper and lower whiskers span the range of data up to 1.5× of the IQR. *$P < 0.05$, ****$P < 0.0001$.

and stem-like memory (Tscm, CCR7$^+$CD45RA$^+$CD95$^+$) phenotypes (Fig. 6D). Recognition of CMV epitopes was additionally associated with expression of GzmB (Fig. 6D).

When grouped into nonreactive, mixed, and reactive responses, we observed that CD8 co-receptor density was strongly reduced for the majority of nonreactive epitope-specific CD8 T cell responses (Fig. 6E). Additionally, we observed a high propensity for naïve phenotypes (Tn, CCR7$^+$CD45RA$^+$CD95$^-$) among nonreactive epitope-specific CD8 T cells (Fig. 6E), which was not explained by nonspecific binding as phenotypic enrichment compared to bulk CD8 T cells was evident (fig. S4C). This is consistent with prior literature showing that naïve CD8 T cells can exhibit reduced TCR sensitivity due to low surface expression of the CD8 co-receptor (*18*). The lack of reactivity among naïve CD8 T cells also aligns with previous description of anergic MART-1-ELAGIGILTV specific T cells in healthy (non-vitiligo, non-melanoma) donors (*21*, *42*). We additionally observed increased proportion of Tem cells among reactive epitope-specific CD8 T cells and a reduced proportion among mixed and nonreactive epitope-specific CD8 T cells (Fig. 6E). Tcm cells and effector memory T cells re-expression CD45RA (Temra, CCR7$^-$CD45RA$^+$) populations were

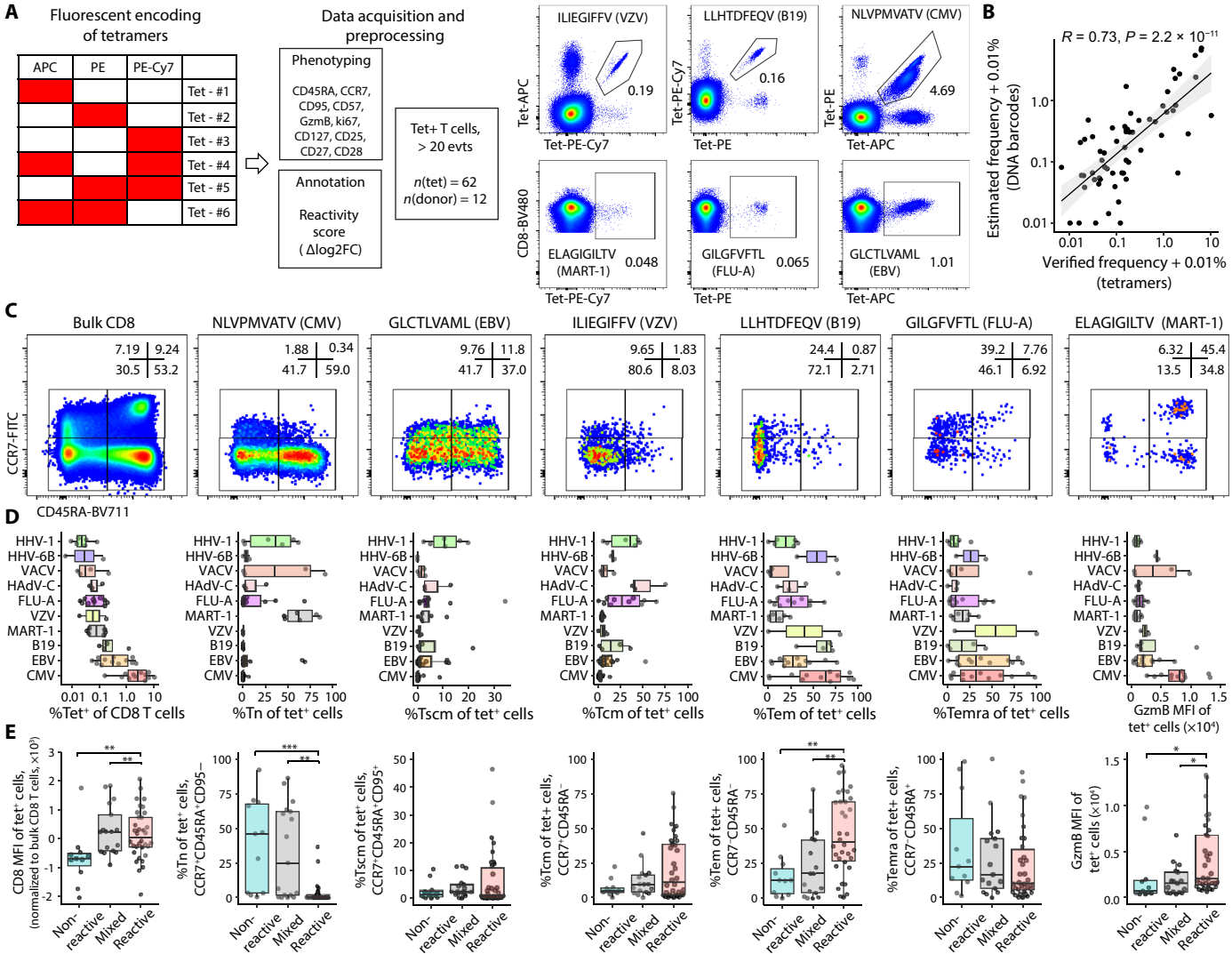

Fig. 6. Differences in antigen reactivity reflect co-receptor expression and effector differentiation. (**A**) Combinatorial encoding of fluorescent pMHC tetramers, experimental setup, and data processing for verification of 62 different epitope-specific CD8 T cell populations across 12 donors. Antigen-specific CD8 T cells for a given fluorophore combination were pregated on CD14$^-$CD19$^-$CD3$^+$CD4$^-$CD8$^+$ T cells negative for irrelevant tetramer fluorophores. Representative tetramer gating is shown from donor 310. (**B**) Correlation between observed frequency measured through DNA-labeled MHC multimers (see Materials and Methods) and verified frequency using fluorescent-labeled tetramers. (**C**) Markers of memory and effector differentiation CCR7 and CD45RA for bulk and tetramer-positive CD8 T cells of donor 310. (**D**) Summary on tetramer frequency, memory phenotypes, and GzmB expression measured by flow cytometry for antigen-specific T cells split by virus origin. (**E**) Quantification of CD8 MFI, Tn, Tscm, Tcm, Tem, Temra, and GzmB MFI for tet$^+$ CD8 T cells grouped by their observed reactivity from initial stimulation and multimer screening. Spearman correlation was performed in (B). *P* values were calculated using Dunn's test and adjusted using the Benjamini-Hochberg method. Boxplot bounds show the 25th and 75th percentiles along with the median. Upper and lower whiskers span the range of data up to 1.5× of the IQR. **P* < 0.05, ***P* < 0.01, ****P* < 0.001. Tet, tetramer. Experiment was performed once.

more evenly distributed among the three categories of antigen reactivity.

We performed FlowSOM clustering (*43*) to further explore phenotypic subsets within nonreactive, mixed, and reactive epitope-specific CD8 T cells. We then generated a two-dimensional representation of phenotypic markers using Uniform Manifold Approximation and Projection (UMAP) (Fig. 7A). Clusters 1 and 2 were identified as memory CD8 T cells with varying degrees of CD127 expression, cluster 3 consisted of GzmB$^+$ Tem cells, clusters 4 and 5 consisted of Ki67$^+$ cycling cells, clusters 6 and 7 consisted of Temra cells, and cluster 8 consisted of naïve CD8 T cells, which were clearly separated from memory CD8 T cells (Fig. 7B). Nonreactive epitope-specific CD8 T cells were again dominated by naïve phenotypes (Fig. 7C). However, two nonreactive epitope-specific CD8 T cells also exhibited high propensity of CD57(hi) Temra phenotypes without expression of CD27 and CD28 (Fig. 7C). This phenotype is consistent with senescent T cell populations that accumulate in aged individuals (*44*). FlowSOM generated clusters that enriched among reactive CD8 T cells included GzmB$^+$ Tems as well CD127$^+$ memory cells (Fig. 7C). GzmB and CD127 were seemingly counter-expressed in our analysis (Fig. 7B). GzmB$^+$ Tem and CD127$^+$ memory cells therefore likely represent two independent subsets with high TCR sensitivity for antigen stimulation.

We additionally examined selected T cell populations based on single-cell transcriptomics. T cell populations were selected based on pMHC multimer binding, sorted and analyzed through the 10x Chromium platform. We assigned pMHC specificity, TCR usage, and transcriptomic features for all captured CD8 T cells. We evaluated 11 different T cell populations and observed that high-frequency T cells with lower mean reactivity (BZLF1-RAKFKQLL) demonstrated distinct phenotype characteristics (*GZMK*, *HLA-DR*, *CD74*, *KLRB1*, and *CRTAM*), while the most reactive T cell populations displayed *GNLY* and *GZMB* expression (fig. S5, A to F).

Together, we conclude that TCR down-regulation and sensitivity to antigen stimulation is associated with distinct T cell phenotypes. Naïve as well as senescent phenotypes associate with reduced TCR sensitivity to antigen stimulation, whereas GzmB$^+$

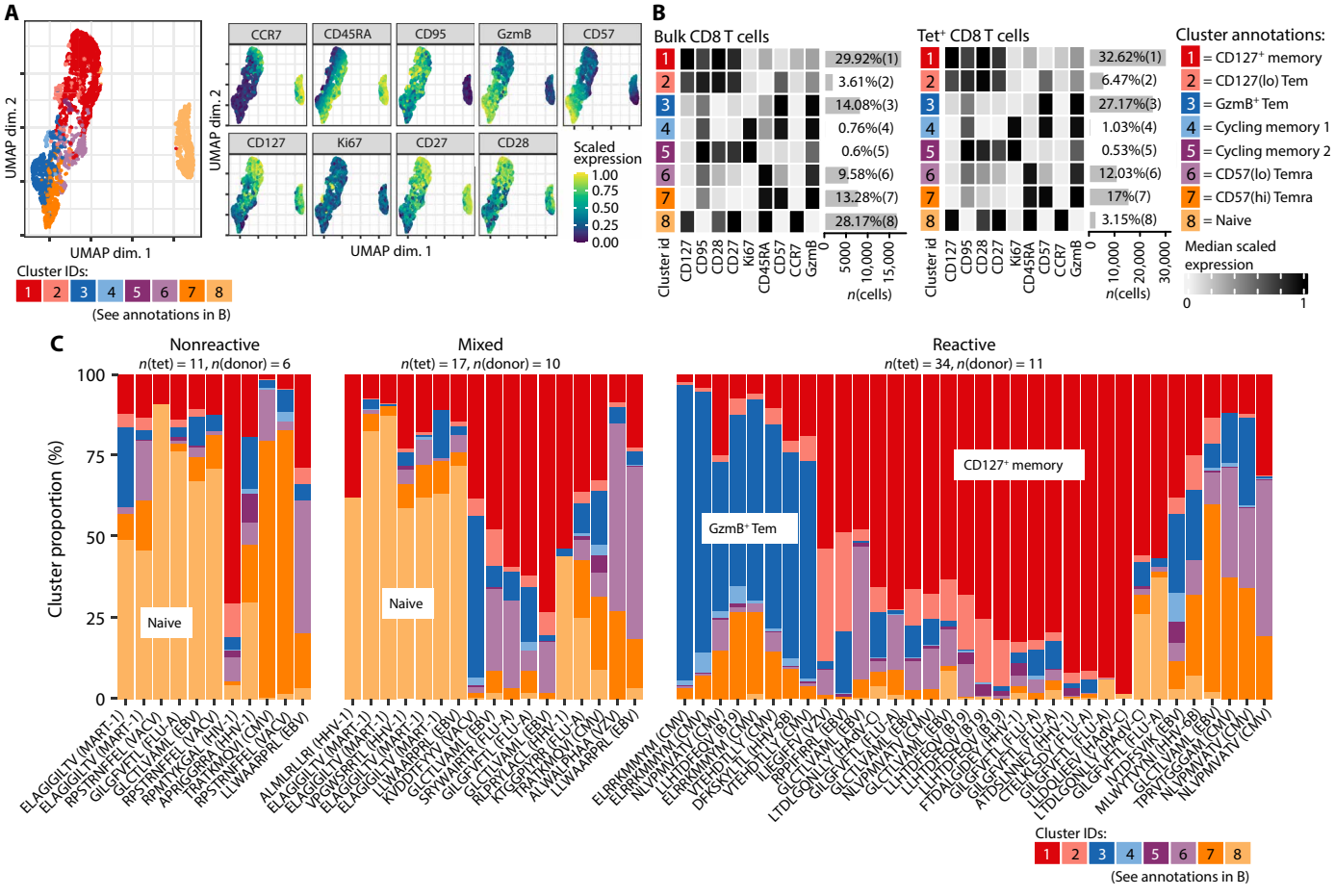

Fig. 7. Differences in antigen reactivity reflect co-receptor expression and effector differentiation. (**A**) Dimensionality reduction of cytometry data from Fig. 6 using flowSOM and UMAP. Maximum 5000 tetramer$^+$ from each population of tetramer$^+$ CD8 T cells, and maximum 5000 bulk CD8 T cells were included from each donor for cluster generation. Maximum 50 random cells from each of tetramer$^+$ and bulk CD8 T cell data files were used for the generation of the UMAP. Marker genes used for FlowSOM clustering are shown along their median scaled expression value. Cluster annotation is shown in (B). (**B**) Heatmaps representing 8 distinct clusters. Eight clusters were used to minimally cover Tn, Tem, and Temra along with cycling cells and CD127$^+$ memory cells (see Materials and Methods). (**C**) Proportion of all eight clusters represented among individual epitope-specific CD8 T cells grouped by response category (nonreactive, mixed, and reactive). Sixty-two tetramer$^+$ populations were included across 12 donors.

Tem cells and CD127^{+} memory cells were highly reactive to antigen stimulation.

DISCUSSION

A reference map of commonly recognized epitopes is necessary and important given the association between the size of the functional antiviral CD8 T cell response and virus control (*45*–*48*). However, recent evidence also point to virus-specific CD8 T cells recognizing common virus infections as bystanders, as well as suspected modulators of pathology, in various disease contexts classically regarded to not involve virus infections including Alzheimer's disease (*49*), hepatitis virus A infection (*50*), and many human tumors (*51*). Here, our reference list of epitopes could be used to elucidate epitope targets and activity of bystander T cells to better understand their disease modulating behavior. Furthermore, bystander CD8 T cells can also serve as therapeutic targets of reactivation as shown by Rosato *et al.* (*51*), making our list potentially suited for translational application in cancer immunotherapy as well.

A concise list of commonly recognized epitopes could moreover prove useful for further characterization of how different environmental exposures affect the antigen-specific repertoire and phenotype of bystander-specific CD8 T cells as we age—including but not limited to the definition of T cell–intrinsic transcriptomic programs involved in memory attrition of bystander-specific CD8 T cells during chronic virus infection as is known from various murine models (*37*, *39*, *40*).

We present a method that allows the separation of T cell populations based of their capacity to respond to antigen stimulation, in large pools of peptides, while retaining the pMHC-specific recognition information. By applying this method, a deeper knowledge can be achieved related to T cell responsiveness in a given donor. Ranking each epitope according to the observed prevalence of reactivity allowed us to further explore phenotypic heterogeneity between antigen-specific populations of CD8 T cells, revealing that nonreactive epitope-specific populations, in addition to senescent Temra-like phenotypes, were associated with CD8^{lo}, naïve-like phenotypes, consistent with prior literature from mice that naïve CD8 T cells downregulate CD8 expression and TCR sensitivity through a process of "co-receptor tuning" (*18*). Given that the loss of CD8 co-receptor expression was evident and uniform for the majority of observed nonreactive populations, we speculate that the same phenomenon may occur for Temra-like CD8 T cells expressing CD57 and CD45RA while lacking CCR7, CD27, and CD28. These hallmarks, as well as *GZMK* expression, are consistent with replicative senescence (*44*).

There is a general association between T cell reactivity and T cell phenotype, but some phenotypes can result in different functional signatures; e.g., the Temra CD57^{hi} population is represented in both reactive and nonreactive T cell pools. The difference observed between functional and nonfunctional Temra CD57^{hi} populations could potentially be further elucidated based on the infection and vaccination history of our donors; however, such information was unavailable, and for most donors, it will be highly diverse, given the breadth of viruses that we are covering. Thus, here, we cannot relate the infection history to the T cell phenotype and reactivity observations made.

The capture of nonreactive T cell populations could additionally arise from non–TCR-driven pMHC binding. It has been demonstrated that MHC multimer binding can occur through non–TCR-driven receptor:ligand interactions with the pMHC molecule; e.g., NK receptors are known to show some peptide preferences in their binding to HLA class I (*52*). Here, however, the characteristics observed in the nonreactive T cell pool associated mostly with these being naïve or Temra CD57^{hi} and directed to viruses and epitopes where limited exposure is expected, such as VACV, MART-1, and NY-ESO. Furthermore, all nonreactive populations displayed a distinct peptide-specific recognition pattern, which is rarely the case for TCR-independent binding.

Our study highlights two biases related to manually curated epitope databases such as IEDB: (i) prevalence of recognition in actual cohort does not correlate with frequency by which each epitope has been studied, and (ii) knowledge on adaptive T cell immunology continues to be biased toward epitopes restricted to HLA-A*02:01. A large number of unrecognized epitopes from common virus infections restricted to non-HLA A*02:01 alleles consequently await exploration, e.g., in the context of HAdV-C, B19, and JCPyV virus, which had comparable reactivity profiles to FLU-A, EBV, and CMV. A broader range of epitopes restricted by more HLA alleles will need to be assessed in future studies to understand potential within-host heterogeneity and to enable studies in ethnically diverse populations with low HLA A*02:01 frequency. A limitation to this study was that all samples from hepatitis donors as well as 11 of 27 healthy donors were taken before October 2019 predating the COVID-19 pandemic and hence not evaluated for severe acute respiratory syndrome coronavirus 2 (SARS-CoV-2) T cell reactivity. Nevertheless, epitope data using binding as an exclusive metric for epitope identification are available for SARS-CoV-2 using similar protocols as presented here (*53*).

MATERIALS AND METHODS

Donor material

Whole blood from 27 anonymous blood donors were obtained at the central blood bank at Rigshospitalet, Copenhagen, and enriched for PBMCs using density centrifugation in Leucosep tubes before cryopreservation at −150°C in fetal bovine serum plus 10% dimethyl sulfoxide (DMSO) PBMCs from 21 patients with hepatitis were collected and cryopreserved under protocol ID #1999-P004983 "Cell Mediated Immunity in Viral hepatitis". We selected 21 samples from a repository with HLA-typed specimens from over 2000 individuals with viral hepatitis, based on the expression of rarer HLA types represented in our multimer library, and to represent diverse age groups, 10 patients above 60 and 10 patients below 30 were selected for investigation. The samples was derived from 11 female and 10 male donors, 20 had HCV and 1 had HBV infection, based on serological and virological testing. Of the participants with HCV, 13 had long-term chronic infection (age 25 to 73, median 62, three treatment experienced with one sustained virological response) and 7 were within the first year of HCV infection (age 19 to 26, mean 24). HCV-positive donors were not investigated for HCV CD8 T cell reactivity but included due to the age-controlled information in this cohort. For anonymous blood donors, HLA information were obtained through NGS typing services at DKMS Life Science Lab GbmH (Dresden, Germany). For patients with hepatitis, HLA typing was obtained through services at University of Oklahoma Health Sciences Center typing. All samples from hepatitis donors as well as 11 of 27 healthy donors were taken before October 2019 predating the COVID-19 pandemic. Additional serology was not performed to determine infection status for common virus infections. All patients and healthy donors provided informed consent before sampling and according to the principles of the Declaration of Helsinki.

Assembly of DNA barcode-labeled dextran multimer libraries

See Supplementary Methods for details on epitope selection. Assembly of DNA barcode-labeled dextran multimer libraries was performed using biotinylated combinatorial DNA barcodes (*24*) (LGC Biosearch, 2.17 μM), fluorescent streptavidin-dextran conjugates (Fina Biosolutions Inc., 160 nM), and custom recombinant, biotinylated, UV-cleavable pMHC monomers (50 μg/ml or approximately 1 μM). Fluorescent dextran conjugates were centrifuged twice at 10,000*g* (2 min, 4°C) to remove aggregates, followed by preincubation with biotinylated DNA barcodes for 30 min at 4°C at a molar ratio of 0.5 DNA barcodes per dextran. Peptide-loaded pMHC monomers were subsequently spun at 3300*g*, 4°C, 5 min, before the addition of supernatant to barcoded dextran conjugates at a molar ratio of 16 to 18 pMHC monomers per dextran. Finally, a premixed freezing buffer was added to a final concentration of phosphate-buffered saline (PBS), 1.5 μM D-biotin, 0.1 mg/ml Herring-DNA, 0.5% bovine serum albumin, 2 mM EDTA, and 5% glycerol. Assembled, DNA barcode-labeled multimers were incubated for 20 min at 4°C before storage at −20°C. The initial concentration of dextran backbone was 160 nM and the final concentration of the assembled multimer was 35.56 nM before staining. See Supplementary Methods for further details.

Pooled peptide stimulation

HLA-restricted peptide pools were generated using a liquid handling robot and stored at −20°C until needed. Donor-specific pools were generated on the day of stimulation with 10 μM of each peptide, and used at a final concentration of 1 μM. Cryopreserved PBMCs were thawed using X-Vivo 15 and 5% human serum. All samples were washed twice in 10 ml of media before 2 to 3 million PBMCs were added to PBS-diluted peptides or equimolar DMSO controls.

Flow cytometry and sorting of multimer-binding CD8 T cells

A total of 1.5 μl of each assembled DNA barcode-labeled multimer was pooled for every stain. Two staining reactions were prepared for each donor. Multimers were first pooled in HLA-restricted pools and subsequently divided into HLA-matching, patient-specific multimer pools. Multimer pools were then concentrated and spun twice to remove aggregates before staining each stimulated/unstimulated sample for 15 min at 37°C followed by labeling with surface antibodies and viability dyes at 4°C. See Supplementary Methods for further details on staining with DNA barcode-labeled multimers as well as combinatorial encoded fluorescent tetramers.

Amplicon sequencing

Co-attached DNA barcodes from sorted antigen-specific populations were amplified using *Taq* polymerase and sample-indexed primers as described previously (*24*); see Supplementary Methods for details and supplemental table 3 for PCR primers.

Sequence analysis

Sequence analysis to calculate significantly enriched DNA barcodes after cell sorting was run as previously described (*24*) using the Barracoda 1.8 web service (https://services.healthtech.dtu.dk/service.php?Barracoda-1.8). See Supplementary Methods for a detailed description of the Barracoda pipeline.

Computational analysis of flow cytometry data

A number of tetramer$^+$ cells were evaluated using FlowJo and compensated fluorescence intensities were exported for each tetramer$^+$ population with more than 20 tetramer$^+$ cells. A maximum of 5000 cells were exported from each CD14$^-$CD19$^-$CD3$^+$CD4$^-$CD8$^+$ tetramer$^+$ population. Each tetramer$^+$ population was enumerated after exclusion of other tetramer-associated fluorescent colors. A total of 5000 cells were also exported from each population of bulk CD8 T cells. The R package CATALYST (*54*, *55*) and flowcore (*56*) were used for processing before annotation and conversion to a SingleCellExperiment object where UMAP and flowSOM analysis was performed. CD45RA, CCR7, CD95, CD127, GzmB, CD57, Ki67, CD27, CD28, and GzmB were selected for clustering. CD25, CD4, CD3, CD8, tetramer-dedicated channels, CD14, NIR, and CD19 were deselected. Eight clusters were chosen for flowSOM clustering, as an elbow plot featured loss of information at eight clusters along with a suitable resolution of memory, effector, and naïve subsets.

Statistical analysis

Flow analysis was done with FlowJo v10.8.1. FlowJo tables and Barracoda outputs were merged and processed for statistical analysis and visualization in R v4.0.5. All correlation plots used Spearman correlations, all two-sample comparisons are performed using Wilcoxon test. Omnibus tests were done using Kruskal-Wallis test, and post hoc analysis among multiple groups was performed using Dunn's test with correction for multiple hypothesis testing using Benjamini-Hochberg. All experiments were performed once using multiple technical controls or biological replicates as stated in the figure texts.

Supplementary Materials

This PDF file includes:

Supplementary Materials and Methods
Table S5
Figs. S1 to S5
Legends for tables S1 to S4
References

Other Supplementary Material for this manuscript includes the following:

Tables S1 to S4

REFERENCES AND NOTES

1. A. Sette, J. Sidney, S. Crotty, T cell responses to SARS-CoV-2. *Annu. Rev. Immunol.* **41**, 343–373 (2023).
2. S. Sridhar, S. Begom, A. Bermingham, K. Hoschler, W. Adamson, W. Carman, T. Bean, W. Barclay, J. J. Deeks, A. Lalvani, Cellular immune correlates of protection against symptomatic pandemic influenza. *Nat. Med.* **19**, 1305–1312 (2013).
3. S. Adamo, Y. Gao, T. Sekine, A. Mily, J. Wu, E. Storgärd, V. Westergren, F. Filén, C. J. Treutiger, J. K. Sandberg, M. Sällberg, P. Bergman, S. Llewellyn-Lacey, H. G. Ljunggren, D. A. Price, A. M. Ekström, A. Sette, A. Grifoni, M. Buggert, Memory profiles distinguish cross-reactive and virus-specific T cell immunity to mpox. *Cell Host Microbe* **31**, 928–936.e4 (2023).
4. N. P. Kristensen, C. Heeke, S. A. Tvingsholm, A. Borch, A. Draghi, M. D. Crowther, I. Carri, K. K. Munk, J. S. Holm, A. M. Bjerregaard, A. K. Bentzen, A. M. Marquard, Z. Szallasi, N. McGranahan, R. Andersen, M. Nielsen, G. B. Jönsson, M. Donia, I. M. Svane, S. R. Hadrup, Neoantigen-reactive CD8+ T cells affect clinical outcome of adoptive cell therapy with tumor-infiltrating lymphocytes in melanoma. *J. Clin. Invest.* **132**, 1–16 (2022).
5. S. A. Rosenberg, N. P. Restifo, Adoptive cell transfer as personalized immunotherapy for human cancer. *Science* **348**, 62–68 (2015).
6. A. D. Waldman, J. M. Fritz, M. J. Lenardo, A guide to cancer immunotherapy: From T cell basic science to clinical practice. *Nat. Rev. Immunol.* **20**, 651–668 (2020).
7. T. N. Schumacher, W. Scheper, P. Kvistborg, Cancer neoantigens. *Annu. Rev. Immunol.* **37**, 173–200 (2019).
8. L. A. Rojas, Z. Sethna, K. C. Soares, C. Olcese, N. Pang, E. Patterson, J. Lihm, N. Ceglia, P. Guasp, A. Chu, R. Yu, A. K. Chandra, T. Waters, J. Ruan, M. Amisaki, A. Zebboudj, Z. Odgerel, G. Payne, E. Derhovanessian, F. Müller, I. Rhee, M. Yadav, A. Dobrin,

M. Sadelain, M. Łuksza, N. Cohen, L. Tang, O. Basturk, M. Gönen, S. Katz, R. K. Do, A. S. Epstein, P. Momtaz, W. Park, R. Sugarman, A. M. Varghese, E. Won, A. Desai, A. C. Wei, M. I. D'Angelica, T. P. Kingham, I. Mellman, T. Merghoub, J. D. Wolchok, U. Sahin, Ö. Türeci, B. D. Greenbaum, W. R. Jarnagin, J. Drebin, E. M. O'Reilly, V. P. Balachandran, Personalized RNA neoantigen vaccines stimulate T cells in pancreatic cancer. *Nature* **618**, 144–150 (2023).
9. A. V. Joglekar, G. Li, T cell antigen discovery. *Nat. Methods* **18**, 873–880 (2021).
10. A. Grifoni, D. Weiskopf, S. I. Ramirez, J. Mateus, J. M. Dan, C. R. Moderbacher, S. A. Rawlings, A. Sutherland, L. Premkumar, R. S. Jadi, D. Marrama, A. M. de Silva, A. Frazier, A. F. Carlin, J. A. Greenbaum, B. Peters, F. Krammer, D. M. Smith, S. Crotty, A. Sette, Targets of T cell responses to SARS-CoV-2 coronavirus in humans with COVID-19 disease and unexposed individuals. *Cell* **181**, 1489–1501.e15 (2020).
11. A. Tarke, J. Sidney, C. K. Kidd, J. M. Dan, S. I. Ramirez, E. D. Yu, J. Mateus, R. da Silva Antunes, E. Moore, P. Rubiro, N. Methot, E. Phillips, S. Mallal, A. Frazier, S. A. Rawlings, J. A. Greenbaum, B. Peters, D. M. Smith, S. Crotty, D. Weiskopf, A. Grifoni, A. Sette, Comprehensive analysis of T cell immunodominance and immunoprevalence of SARS-CoV-2 epitopes in COVID-19 cases. *Cell Reports Med.* **2**, 100204 (2021).
12. M. Wolfl, W. Y. Ho, H. Nguyen, T. J. Manley, M. Bleakley, P. D. Greenberg, Activation-induced expression of CD137 permits detection, isolation, and expansion of the full repertoire of CD8+ T cells responding to antigen without requiring knowledge of epitope specificities. *Immunobiology* **110**, 201–210 (2007).
13. L. Lamoreaux, M. Roederer, R. Koup, Intracellular cytokine optimization and standard operating procedure. *Nat. Protoc.* **1**, 1507–1516 (2006).
14. M. McCutcheon, N. Wehner, A. Wensky, M. Kushner, S. Doan, L. Hsiao, P. Calabresi, T. Ha, T. V. Tran, K. M. Tate, J. Winkelhake, E. G. Spack, A sensitive ELISPOT assay to detect low-frequency human T lymphocytes. *J. Immunol. Methods* **210**, 149–166 (1997).
15. L. V. Sibener, R. A. Fernandes, E. M. Kolawole, C. B. Carbone, F. Liu, D. McAffee, M. E. Birnbaum, X. Yang, L. F. Su, W. Yu, S. Dong, M. H. Gee, K. M. Jude, M. M. Davis, J. T. Groves, W. A. Goddard, J. R. Heath, B. D. Evavold, R. D. Vale, K. C. Garcia, Isolation of a structural mechanism for uncoupling T cell receptor signaling from peptide-MHC binding. *Cell* **174**, 672–687.e27 (2018).
16. J. J. Adams, S. Narayanan, B. Liu, M. E. Birnbaum, A. C. Kruse, N. A. Bowerman, W. Chen, A. M. Levin, J. M. Connolly, C. Zhu, D. M. Kranz, K. C. Garcia, T cell receptor signaling is limited by docking geometry to peptide-major histocompatibility complex. *Immunity* **35**, 681–693 (2011).
17. R. Vazquez-Lombardi, J. S. Jung, F. S. Schlatter, A. Mei, N. R. Mantuano, F. Bieberich, K. L. Hong, J. Kucharczyk, E. Kapetanovic, E. Aznauryan, C. R. Weber, A. Zippelius, H. Läubli, S. T. Reddy, High-throughput T cell receptor engineering by functional screening identifies candidates with enhanced potency and specificity. *Immunity* **55**, 1953–1966.e10 (2022).
18. J. H. Park, S. Adoro, P. J. Lucas, S. D. Sarafova, A. S. Alag, L. L. Doan, B. Erman, X. Liu, W. Ellmeier, R. Bosselut, L. Feigenbaum, A. Singer, "Coreceptor tuning": Cytokine signals transcriptionally tailor CD8 coreceptor expression to the self-specificity of the TCR. *Nat. Immunol.* **8**, 1049–1059 (2007).
19. J. Pettmann, A. Huhn, E. A. Shah, M. A. Kutuzov, D. B. Wilson, M. L. Dustin, S. J. Davis, P. A. van der Merwe, O. Dushek, The discriminatory power of the T cell receptor. *eLife* **10**, 1–42 (2021).
20. P. D. Holler, D. M. Kranz, Quantitative analysis of the contribution of TCR/pepMHC affinity and CD8 to T cell activation. *Immunity* **18**, 255–264 (2003).
21. Y. Maeda, H. Nishikawa, D. Sugiyama, D. Ha, M. Hamaguchi, T. Saito, M. Nishioka, J. B. Wing, D. Adeegbe, I. Katayama, S. Sakaguchi, Detection of self-reactive CD8+ T cells with an anergic phenotype in healthy individuals. *Science* **346**, 1536–1540 (2014).
22. J. Carnevale, E. Shifrut, N. Kale, W. A. Nyberg, F. Blaeschke, Y. Y. Chen, Z. Li, S. P. Bapat, M. E. Diolaiti, P. O'Leary, S. Vedova, J. Belk, B. Daniel, T. L. Roth, S. Bachl, A. A. Anido, B. Prinzing, J. Ibañez-Vega, S. Lange, D. Haydar, M. Luetke-Eversloh, M. Born-Bony, B. Hegde, S. Kogan, T. Feuchtinger, H. Okada, A. T. Satpathy, K. Shannon, S. Gottschalk, J. Eyquem, G. Krenciute, A. Ashworth, A. Marson, RASA2 ablation in T cells boosts antigen sensitivity and long-term function. *Nature* **609**, 174–182 (2022).
23. R. Vita, S. Mahajan, J. A. Overton, S. K. Dhanda, S. Martini, J. R. Cantrell, D. K. Wheeler, A. Sette, B. Peters, The immune epitope database (IEDB): 2018 update. *Nucleic Acids Res.* **47**, D339–D343 (2019).
24. A. K. Bentzen, A. M. Marquard, R. Lyngaa, S. K. Saini, S. Ramskov, M. Donia, L. Such, A. J. S. Furness, N. McGranahan, R. Rosenthal, P. T. Straten, Z. Szallasi, I. M. Svane, C. Swanton, S. A. Quezada, S. N. Jakobsen, A. C. Eklund, S. R. Hadrup, Large-scale detection of antigen-specific T cells using peptide-MHC-I multimers labeled with DNA barcodes. *Nat. Biotechnol.* **34**, 1037–1045 (2016).
25. A. Tarke, J. Sidney, N. Methot, E. D. Yu, Y. Zhang, J. M. Dan, B. Goodwin, P. Rubiro, A. Sutherland, E. Wang, A. Frazier, S. I. Ramirez, S. A. Rawlings, D. M. Smith, R. da Silva Antunes, B. Peters, R. H. Scheuermann, D. Weiskopf, S. Crotty, A. Grifoni, A. Sette, Impact of SARS-CoV-2 variants on the total CD4+ and CD8+ T cell reactivity in infected or vaccinated individuals. *Cell Reports Med.* **2**, 100355 (2021).
26. S. Q. Zhang, K. Y. Ma, A. A. Schonnesen, M. Zhang, C. He, E. Sun, C. M. Williams, W. Jia, N. Jiang, High-throughput determination of the antigen specificities of T cell receptors in single cells. *Nat. Biotechnol.* **36**, 1156–1159 (2018).
27. A. K. Bentzen, L. Such, K. K. Jensen, A. M. Marquard, L. E. Jessen, N. J. Miller, C. D. Church, R. Lyngaa, D. M. Koelle, J. C. Becker, C. Linnemann, T. N. M. Schumacher, P. Marcatili, P. Nghiem, M. Nielsen, S. R. Hadrup, T cell receptor fingerprinting enables in-depth characterization of the interactions governing recognition of peptide–MHC complexes. *Nat. Biotechnol.* **36**, 1191–1196 (2018).
28. T. Kivioja, A. Väharautio, K. Karlsson, M. Bonke, M. Enge, S. Linnarsson, J. Taipale, Counting absolute numbers of molecules using unique molecular identifiers. *Nat. Methods* **9**, 72–74 (2012).
29. Z. Cai, H. Kishimoto, A. Brunmark, M. R. Jackson, P. A. Peterson, J. Sprent, Requirements for peptide-induced T cell receptor downregulation on naive CD8+ T cells. *J. Exp. Med.* **185**, 641–652 (1997).
30. S. Valitutti, S. Müller, M. Cella, E. Padovan, A. Lanzavecchia, Serial triggering of many T-cell receptors by a few peptide-MHC complexes. *Nature* **375**, 148–151 (1995).
31. C. M. Bonefeld, A. B. Rasmussen, J. P. H. Lauritsen, M. von Essen, N. Ødum, P. S. Andersen, C. Geisler, TCR comodulation of nonengaged TCR takes place by a protein kinase C and CD3γ Di-leucine-based motif-dependent mechanism. *J. Immunol.* **171**, 3003–3009 (2003).
32. C. Kao, M. A. Daniels, S. C. Jameson, Loss of CD8 and TCR binding to Class I MHC ligands following T cell activation. *Int. Immunol.* **17**, 1607–1617 (2005).
33. Y. F. Fuchs, V. Sharma, A. Eugster, G. Kraus, R. Morgenstern, A. Dahl, S. Reinhardt, A. Petzold, A. Lindner, D. Löbel, E. Bonifacio, Gene expression-based identification of antigen-responsive CD8+ T cells on a single-cell level. *Front. Immunol.* **10**, 1–15 (2019).
34. C. Alanio, F. Lemaitre, H. K. W. Law, M. Hasan, M. L. Albert, Enumeration of human antigen-specific naive CD8+ T cells reveals conserved precursor frequencies. *Blood* **115**, 3718–3725 (2010).
35. P. G. Coulie, B. J. Van Den Eynde, P. Van Der Bruggen, T. Boon, Tumour antigens recognized by T lymphocytes: At the core of cancer immunotherapy. *Nat. Rev. Cancer* **14**, 135–146 (2014).
36. B. Reynisson, B. Alvarez, S. Paul, B. Peters, M. Nielsen, NetMHCpan-4.1 and NetMHCIIpan-4.0: Improved predictions of MHC antigen presentation by concurrent motif deconvolution and integration of MS MHC eluted ligand data. *Nucleic Acids Res.* **48**, W449–W454 (2021).
37. I. Barnstorf, S. P. M. Welten, M. Borsa, N. S. Baumann, K. Pallmer, N. Joller, R. Spörri, A. Oxenius, Chronic viral infections impinge on naive bystander CD8 T cells. *Inflamm. Dis.* **8**, 249–257 (2020).
38. S.-K. Kim, R. M. Welsh, Comprehensive early and lasting loss of memory CD8 T cells and functional memory during acute and persistent viral infections. *J. Immunol.* **172**, 3139–3150 (2004).
39. I. Barnstorf, M. Borsa, N. Baumann, K. Pallmer, A. Yermanos, N. Joller, R. Spörri, S. P. M. Welten, N. J. Kräutler, A. Oxenius, Chronic virus infection compromises memory bystander T cell function in an IL-6/ STAT1-dependent manner. *J. Exp. Med.* **216**, 571–586 (2019).
40. E. Stelekati, H. Shin, T. A. Doering, D. V. Dolfi, C. G. Ziegler, D. P. Beiting, L. Dawson, J. Liboon, D. Wolski, M. A. A. Ali, P. D. Katsikis, H. Shen, D. S. Roos, W. N. Haining, G. M. Lauer, E. J. Wherry, Bystander chronic infection negatively impacts development of CD8+ T cell memory. *Immunity* **40**, 801–813 (2014).
41. C. L. Gordon, M. Miron, J. J. C. Thome, N. Matsuoka, J. Weiner, M. A. Rak, S. Igarashi, T. Granot, H. Lerner, F. Goodrum, D. L. Farber, Tissue reservoirs of antiviral T cell immunity in persistent human CMV infection. *J. Exp. Med.* **214**, 651–667 (2017).
42. M. J. Pittet, D. Valmori, P. R. Dunbar, D. E. Speiser, D. Liénard, F. Lejeune, K. Fleischhauer, V. Cerundolo, J. C. Cerottini, P. Romero, High frequencies of naive Melan-A/MART-1-specific CD8+ T cells in a large proportion of human histocompatibility leukocyte antigen (HLA)-A2 individuals. *J. Exp. Med.* **190**, 705–716 (1999).
43. S. Van Gassen, B. Callebaut, M. J. Van Helden, B. N. Lambrecht, P. Demeester, T. Dhaene, Y. Saeys, FlowSOM: Using self-organizing maps for visualization and interpretation of cytometry data. *Cytom. Part A* **87**, 636–645 (2015).
44. G. Soto-Heredero, M. M. G. de Las Heras, J. I. Escrig-Larena, M. Mittelbrunn, Extremely differentiated T cell subsets contribute to tissue deterioration during aging. *Annu. Rev. Immunol.* **41**, 181–205 (2023).
45. C. L. Day, D. E. Kaufmann, P. Kiepiela, J. A. Brown, E. S. Moodley, S. Reddy, E. W. Mackey, J. D. Miller, A. J. Leslie, C. DePierres, Z. Mncube, J. Duraiswamy, B. Zhu, Q. Eichbaum, M. Altfeld, E. J. Wherry, H. M. Coovadia, P. J. R. Goulder, P. Klenerman, R. Ahmed, G. J. Freeman, B. D. Walker, PD-1 expression on HIV-specific T cells is associated with T-cell exhaustion and disease progression. *Nature* **443**, 350–354 (2006).
46. D. L. Barber, E. J. Wherry, D. Masopust, B. Zhu, J. P. Allison, A. H. Sharpe, G. J. Freeman, R. Ahmed, Restoring function in exhausted CD8 T cells during chronic viral infection. *Nature* **439**, 682–687 (2006).
47. L. Rivino, N. Le Bert, U. S. Gill, K. Kunasegaran, Y. Cheng, D. Z. M. Tan, E. Becht, N. K. Hansi, G. R. Foster, T. H. Su, T. C. Tseng, S. G. Lim, J. H. Kao, E. W. Newell, P. T. F. Kennedy, A. Bertoletti, Hepatitis b virus–specific T cells associate with viral control upon nucleos(t) ide-analogue therapy discontinuation. *J. Clin. Invest.* **128**, 668–681 (2018).
48. M. R. Betts, M. C. Nason, S. M. West, S. C. De Rosa, S. A. Migueles, J. Abraham, M. M. Lederman, J. M. Benito, P. A. Goepfert, M. Connors, M. Roederer, R. A. Koup, HIV

nonprogressors preferentially maintain highly functional HIV-specific CD8+ T cells. *Blood* **107**, 4781–4789 (2006).
49. D. Gate, N. Saligrama, O. Leventhal, A. C. Yang, M. S. Unger, J. Middeldorp, K. Chen, B. Lehallier, D. Channappa, M. B. De Los Santos, A. McBride, J. Pluvinage, F. Elahi, G. K. Y. Tam, Y. Kim, M. Greicius, A. D. Wagner, L. Aigner, D. R. Galasko, M. M. Davis, T. Wyss-Coray, Clonally expanded CD8 T cells patrol the cerebrospinal fluid in Alzheimer's disease. *Nature* **577**, 399–404 (2020).
50. J. Kim, D. Y. Chang, H. W. Lee, H. Lee, J. H. Kim, P. S. Sung, K. H. Kim, S. H. Hong, W. Kang, J. Lee, S. Y. Shin, H. T. Yu, S. You, Y. S. Choi, I. Oh, D. H. Lee, D. H. Lee, M. K. Jung, K. S. Suh, S. Hwang, W. Kim, S. H. Park, H. J. Kim, E. C. Shin, Innate-like cytotoxic function of bystander-activated CD8+ T cells is associated with liver injury in acute hepatitis A. *Immunity* **48**, 161–173.e5 (2018).
51. P. C. Rosato, S. Wijeyesinghe, J. M. Stolley, C. E. Nelson, R. L. Davis, L. S. Manlove, C. A. Pennell, B. R. Blazar, C. C. Chen, M. A. Geller, V. Vezys, D. Masopust, Virus-specific memory T cells populate tumors and can be repurposed for tumor immunotherapy. *Nat. Commun.* **10**, (2019).
52. J. C. Boyington, S. A. Motyka, P. Schuck, A. G. Brooks, P. D. Sun, Crystal structure of an NK cell immunoglobulin-like receptor in complex with its class I MHC ligand. *Nature* **405**, 537–543 (2000).
53. S. K. Saini, D. S. Hersby, T. Tamhane, H. R. Povlsen, S. P. Amaya Hernandez, M. Nielsen, A. O. Gang, S. R. Hadrup, SARS-CoV-2 genome-wide T cell epitope mapping reveals immunodominance and substantial CD8+ T cell activation in COVID-19 patients. *Sci. Immunol.* **6**, 1–16 (2021).
54. S. Chevrier, H. L. Crowell, V. R. T. Zanotelli, S. Engler, M. D. Robinson, B. Bodenmiller, Compensation of signal spillover in suspension and imaging mass cytometry. *Cell Syst.* **6**, 612–620.e5 (2018).
55. M. Nowicka, C. Krieg, H. L. Crowell, L. M. Weber, F. J. Hartmann, S. Guglietta, B. Becher, M. P. Levesque, M. D. Robinson, CyTOF workflow: Differential discovery in high-throughput high-dimensional cytometry datasets. *F1000research* , 1–56 (2019).
56. F. Hahne, N. Lemeur, R. R. Brinkman, B. Ellis, P. Haaland, D. Sarkar, J. Spidlen, E. Strain, R. Gentleman, flowCore: A bioconductor package for high throughput flow cytometry. *BMC Bioinformatics* **10**, 106 (2009).
57. B. Rodenko, M. Toebes, S. R. Hadrup, W. J. E. van Esch, A. M. Molenaar, T. N. M. Schumacher, H. Ovaa, Generation of peptide–MHC class I complexes through UV-mediated ligand exchange. *Nat. Protoc.* **1**, 1120–1132 (2006).
58. M. Toebes, M. Coccoris, A. Bins, B. Rodenko, R. Gomez, N. J. Nieuwkoop, W. Van De Kasteele, G. F. Rimmelzwaan, J. B. A. G. Haanen, H. Ovaa, T. N. M. Schumacher, Design and use of conditional MHC class I ligands. *Nat. Med.* **12**, 246–251 (2006).
59. S. K. Saini, T. Tamhane, R. Anjanappa, A. Saikia, S. Ramskov, M. Donia, I. M. Svane, S. N. Jakobsen, M. Garcia-Alai, M. Zacharias, R. Meijers, S. Springer, S. R. Hadrup, Empty peptide-receptive MHC class I molecules for efficient detection of antigen-specific T cells. *Sci. Immunol.* **4**, (2019).
60. Q. Xu, M. R. Schlabach, G. J. Hannon, S. J. Elledge, B. Watson, Design of 240,000 orthogonal 25mer DNA barcode probes. *Proc. Natl. Acad. Sci.* **106**, 2289–2294 (2009).
61. R. S. Andersen, P. Kvistborg, T. Mørch Frøsig, N. W. Pedersen, R. Lyngaa, A. H. Bakker, C. J. Shu, P. T. Straten, T. N. Schumacher, S. R. Hadrup, Parallel detection of antigen-specific T cell responses by combinatorial encoding of MHC multimers. *Nat. Protoc.* **7**, 891–902 (2012).
62. M. D. Robinson, D. J. McCarthy, G. K. Smyth, edgeR: A Bioconductor package for differential expression analysis of digital gene expression data. *Bioinformatics* **26**, 139–140 (2009).
63. M. D. Robinson, A. Oshlack, A scaling normalization method for differential expression analysis of RNA-seq data. *Genome Biol.* **11**, R25 (2010).
64. H. R. Povlsen, A. K. Bentzen, M. Kadivar, L. E. Jessen, S. R. Hadrup, M. Nielsen, Improved T cell receptor antigen pairing through data-driven filtering of sequencing information from single cells. *Elife* , e81810 (2023).
65. S. R. Hadrup, A. H. Bakker, C. J. Shu, R. S. Andersen, J. van Veluw, P. Hombrink, E. Castermans, P. T. Straten, C. Blank, J. B. Haanen, M. H. Heemskerk, T. N. Schumacher, Parallel detection of antigen-specific T-cell responses by multidimensional encoding of MHC multimers. *Nat. Methods* **6**, 520–526 (2009).
66. H. Wickham, M. Averick, J. Bryan, W. Chang, L. McGowan, R. François, G. Grolemund, A. Hayes, L. Henry, J. Hester, M. Kuhn, T. Pedersen, E. Miller, S. Bache, K. Müller, J. Ooms, D. Robinson, D. Seidel, V. Spinu, K. Takahashi, D. Vaughan, C. Wilke, K. Woo, H. Yutani, Welcome to the Tidyverse. *J. Open Source Softw.* **4**, 1686 (2019).

Acknowledgments: We thank technical staff B. Rotbøll and A. F. Løye for technical expertise as well as all participating donors. We furthermore thank the Memorial Sloan Kettering Cancer Center and C. Leslie as well as K. Schober from the University Hospital Erlangen for thoughtful commentary and hospitality in closing this manuscript. **Funding:** This work was supported by the European Research Council, the ERC StG NextDART and ERC CoG MIMIC, and the Independent Research Fund, Denmark, EliteForsk grant to N.P.K. and S.R.H., and by Lundbeck Foundation grants (R324-2019-1671 and R322-2019-2445) to A.K.B. **Author contributions:** N.P.K. designed the experiments, optimized the assay, generated data, analyzed experimental data, and wrote the manuscript. E.D. generated experimental data. A.K.B. designed the DNA barcodes, provided consultation, and helped designing and performing experiments. U.K.H. maintained and quality-checked the stock of biotinylated DNA barcodes. T.T. manufactured folded, biotinylated pMHC monomers. J.S.K. generated data and provided analytical assistance. G.N. provided bioinformatics assistance. L.F.V. provided experimental assistance. G.M.L. provided samples and input to data analysis and wrote the manuscript. S.R.H. is the principal investigator, designed experiments, wrote the manuscript, and provided guidance throughout. **Competing interests:** S.R.H. and A.K.B. are coinventors of patents WO2015185067 (Determining antigen recognition through barcoding of MHC multimers) and WO2015188839 (General detection and isolation of specific cells by binding of labeled molecules) for the barcoded MHC technology that is licensed to Immudex. All other authors declare that they have no competing interests. **Data and materials availability:** All data needed to evaluate the conclusions in the paper are present in the paper and/or the Supplementary Materials. In addition, multimodal single-cell sequencing data are available through ArrayExpress at E-MTAB-13758, and flow cytometry data are available at ImmPort (immport.org) under study accession SDY2500.

Submitted 14 November 2023
Accepted 12 March 2024
Published 12 April 2024
10.1126/sciadv.adm8951